Anhydrous Superprotonic Conductivity in the Zirconium Acid Triphosphate $ZrH_5(PO_4)_3$

Sacha Fop,[1,2,*] Riccardo Vivani,[3,4] Silvia Masci,[5] Mario Casciola,[5] Anna Donnadio,[3,4,*]

[1] The Chemistry Department, University of Aberdeen, Aberdeen AB24 3UE, United Kingdom

[2] ISIS Facility, Rutherford Appleton Laboratory, Harwell OX11 0QX, United Kingdom

[3] Department of Pharmaceutical Sciences, University of Perugia, Via del Liceo 1, 06123 Perugia, Italy

[4] CEMIN – Centro di Eccellenza Materiali Innovativi Nanostrutturali per Applicazioni Chimiche, Fisiche e Biomediche, University of Perugia, Via Elce di Sotto 8, 06123, Perugia, Italy

[5] Department of Chemistry, Biology and Biotechnologies, University of Perugia, Via Elce di Sotto 8, 06123 Perugia, Italy

ABSTRACT: The development of solid-state proton conductors with high proton conductivity at low temperature is crucial for the implementation of hydrogen-based technologies for portable and automotive applications. Here, we report on the discovery of a new crystalline tetravalent metal acid triphosphate, $ZrH_5(PO_4)_3$ (ZP3), which exhibits record-high proton conductivity of ~ 3.0 x 10^{-2} S cm^{-1} at 110 °C in anhydrous conditions. Structural characterization and bond-valence sum energy (BVSE) calculations reveal the pathways and mechanism of proton transport. Extended defective hydrogen bond chains, where the protons are dynamically disordered over two oxygen centers, enable fast ionic diffusion with minimal activation energy for proton hopping.

Solid-state proton conductors (SSPCs) are ionic conductors in which the diffusion of H^+ ions is responsible for charge transfer. Depending on their physicochemical characteristics and temperatures of operation, several classes of SSPCs can be identified, [1] with important applications in a range of hydrogen-based energy technologies. [2] SSPCs with target proton conductivity (10^{-2} S cm^{-1}) at low temperatures, such as polymer electrolyte proton conductors, can be used for the development of fuel cells operating at ≤ 150 °C, thus unlocking the utilization of hydrogen for portable and automotive applications. [3] However, polymer electrolytes such as Nafion or other perfluorosulfonated membranes have high costs, show poor mechanical and chemical stability and require to be hydrated (relative humidity, RH, > 90%) to maintain high ionic conductivities. [4] Solid acids based on tetrahedral oxyanion groups like CsH_2PO_4 offer an alternative to polymer electrolytes as they exhibit high proton conductivity at moderate temperatures (100 – 300 °C), due to a polymorphic phase transition to a highly conductive superprotonic phase characterized by highly mobile disordered protons. [5, 6] Although these systems have shown good performances in fuel cells, the use of solid acids as electrolytes has been hindered by their low ionic conductivity below the phase transition, as well as the stability of the superprotonic phase which requires active humidification. [2e, 7, 8] Metal-organic frameworks (MOF) proton conductors can exhibit proton conductivity under anhydrous conditions when impregnated with non-volatile acids (e.g., H_2SO_4 and H_3PO_4) or conducting media (such as organic aryl molecules like triazole and imidazole), although their conductivities and stability are often inadequate for practical applications. [9, 10] The development of new SSPCs with good phase stability and high conductivity in anhydrous conditions, which would avoid the implementation of complex water management systems and allow the use of operation temperatures ≥ 100 °C to improve the electrodes efficiency, is still an open challenge for scientists working on low and moderate temperature fuel cells and hydrogen technologies.

Here, we report on the discovery of a new zirconium acid triphosphate, $ZrH_5(PO_4)_3$ (ZP3), with record-high proton conductivity of ~ 3.0 x 10^{-2} S cm^{-1} at 110 °C in anhydrous conditions (relative humidity RH << 1%, pH_2O << 10^{-2} atm). This value of anhydrous proton conductivity is unprecedent and comparable with benchmark polymer electrolytes and MOF proton conductors operating under high relative humidity. ZP3 does not exhibit any phase transition and maintains high proton conductivity even at room temperature.

Zirconium hydrogen phosphates are a class of Zr(IV) solid acids exhibiting various layered (α-$Zr(HPO_4)_2 \cdot H_2O$, γ-$Zr(PO_4)(H_2PO_4) \cdot 2H_2O$, θ-$Zr(HPO_4)_2 \cdot 8H_2O$) and three-

dimensional (τ- and τ'-$Zr(HPO_4)_2$) crystalline phases which can be formed via control of the P:Zr molar ratio and of the reaction medium and conditions. [11] ZP3 was precipitated by reacting anhydrous $ZrOCl_2$ with excess phosphoric acid (initial P:Zr molar ratio of 25) at 85 °C (see Supplementary Information for further experimental details). The images from scanning electron microscopy (SEM) evidence a cubic-like morphology of the obtained ZP3 crystals (Figure S1), in contrast with the platelet-like shapes reported for layered α- and γ-zirconium phosphate. [11a, 11c]

Inductively coupled plasma optical emission spectroscopy (ICP-OES) measurements indicated a composition of P:Zr = 2.98(5) in agreement with the nominal P:Zr ratio of 3. Results from measurements of NH_3 chemisorption were consistent with the presence of five acidic hydrogen atoms belonging to three phosphate groups. Thermogravimetric (TGA) measurements until full decomposition to the pyrophosphate ZrP_2O_7 gave weight losses consistent with a molecular mass of 375 u (Figure S2), in agreement with the nominal mass of 381 u for the chemical formula of ZP3. These results confirmed that the composition of as prepared ZP3 is $ZrH_5(PO_4)_3$.

Figure 1a shows the X-ray powder diffraction pattern of ZP3. The powder diffraction pattern could be indexed with a trigonal unit cell with lattice parameters *a* = 8.27325(3) Å and *c* = 25.5433(2) Å, with the most probable space group $R\bar{3}c$ (see Supplementary Information). The crystal structure of ZP3 was solved *ab initio* from powder X-ray diffraction data. An initial structural model was determined using the real space global optimization methods implemented in FOX with the parallel tempering algorithm, [12] and subsequently refined with the GSAS/EXPGUI software package. [13] Rietveld refinement of the obtained structural model resulted in an excellent fit to the powder diffraction data (Figure 1a), with good statistical factors and realistic atomic parameters and distances (see Table S1 for the detailed crystal data and Table S2 for selected bond distances and angles). The structure of ZP3 is composed of a three-dimensional network of alternating layers of PO_4 tetrahedra and ZrO_6 octahedra connected via corner sharing (Figure 1b). The phosphate units are constituted by two oxygen atoms shared with two adjacent Zr atoms (O1) and two non-bridging terminal oxygen atoms (O2), which are available to form hydroxyl OH groups. Adjacent non-bridging O2 atoms form a continuous network of equidistant short hydrogen bonds O2–H···O2 (2.756(2) and 2.762(2) Å) (Figure 1c). The solid-state ^{31}P MAS-NMR spectrum of ZP3 shows only one resonance at about -17 ppm, thus indicating the presence of only one type of phosphate group (Figure S3).[14] This implies that the five protons per formula unit of ZP3 are delocalized on six crystallographically equivalent non-coordinated oxygen atoms (two per phosphate group), thus resulting in a partially protonated phosphate group with average composition $PO_2(OH_{0.833})_2$. This creates a series of proton vacancies where a proton of an adjacent OH group can jump on. Such a structural network provides pathways for fast proton transport. [8b, 15]

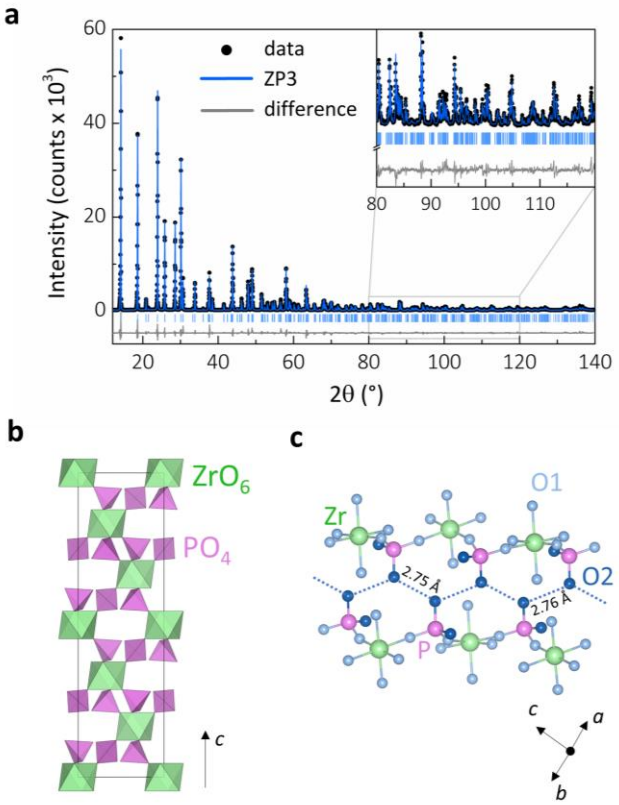

Figure 1. **(a)** Rietveld refinement fit to the powder X-ray diffraction data of ZP3. The vertical marks indicate the calculated reflection positions. **(b)** Crystal structure of ZP3 showing the alternating layers of ZrO_6 octahedra and PO_4 tetrahedra. **(c)** View of the hydrogen-bond network connecting the non-bridging oxygen atoms of adjacent phosphate groups.

The proton conductivity of ZP3 was analyzed by AC impedance spectroscopy. The conductivity measurements were performed on a dense ZP3 pellet sample (~ 93% of the theoretical density) under anhydrous conditions (RH << 1%, $pH_2O << 10^{-2}$ atm) in the temperature range 25 – 120 °C. Stability tests in a range of temperatures and RH values demonstrated that in dry conditions the ZP3 phase is stable over a large temperature window (0 – 120 °C) (Figure S4). This is in stark contrast with the superprotonic phase of CsH_2PO_4, which is only stable in a narrow temperature range under dry conditions. [6, 7, 8, 16] The proton conductivity of ZP3 is presented in Figure 2a. No loss of proton conductivity was observed during two cooling and heating cycles conducted over several hours, and no phase changes were detected from a diffraction pattern collected post-conductivity measurements (Figure S5), thus confirming the good stability of ZP3. Any possible contribution of H_3PO_4 (which could have been formed at the grain boundary during the preparation of the pellet sample) to the proton conductivity of ZP3 can be excluded

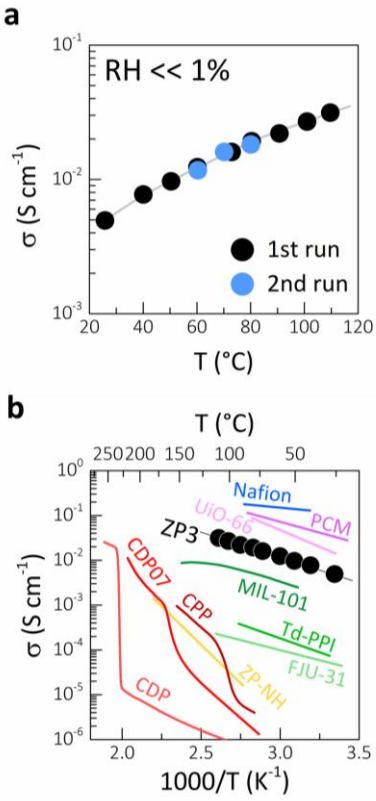

Figure 2. **(a)** Proton conductivity of ZP3 measured under anhydrous conditions (relative humidity RH << 1%, pH_2O << 10^{-2} atm). Data taken over two different cooling and heating cycles is shown for comparison. **(b)** Arrhenius plot of the proton conductivity of ZP3 in anhydrous conditions compared with the conductivities of: Nafion at 90% RH [19]; solid acids CsH_2PO_4 (CDP), $(CsH_2PO_4)_{0.93}(H_3PO_4)_{0.07}$ (CDP07) and $Cs_7(H_4PO_4)(H_2PO_4)_8$ (CPP) (data above 130 °C recorded under active humidification, pH_2O > 0.47 atm) [8]; metal-organic frameworks: H_2SO_4-impregnated Cr(III) terephthalate (MIL-101, anhydrous) [9b], imidazole-loaded tetrahedral polymide (Td-PPI, anhydrous) [9c], hydroquinone-loaded $[Zn_3(tz)_2(bdc)_2]_n$ (FJU-31, anhydrous) [9e], UiO-66-type decorated with sulfonic acid groups (UiO-66, RH 90%) [17a], β-PCMOF2[1/2] doped with triazole (PCM, RH 90%) [20c]; zirconium phosphate with guest NH_4^+ cations $(NH_4)_3[Zr(H_{2/3}PO_4)_3]$ (ZP-NH, anhydrous) [18a].

or estimated to be at most ~ 5% (see Supplementary Information for further details). Therefore, the high ionic conductivity of ZP3 can be ascribed to fast proton transport within the bulk material. Under anhydrous conditions, ZP3 exhibits very high proton conductivity of ~ 0.5 – 3.0 x 10^{-2} S cm^{-1} and activation energy of 0.21(1) eV between 25 and 110 °C, which are in the range of superprotonic conductivity [6, 8, 17]. The conductivity of ZP3 far exceeds the anhydrous proton conductivity values recently reported for zirconium phosphate crystals containing guest NH_4^+ cations (in the range 10^{-5} – 10^{-3} S cm^{-1} between 90 and 230 °C). [18] As shown in the Arrhenius plots in Figure 2b, the conductivity of ZP3 is comparable with the conductivity of the benchmark polymer electrolyte conductor Nafion [19] and of some of the best-performing MOF proton conductors operating under humidified conditions. [17a, 20] The proton conductivity of ZP3 is also 2 – 5 orders of magnitudes higher than the conductivity of CsH_2PO_4-type solid acid conductors. [6, 8] One of the main drawbacks of polymer electrolytes and CsH_2PO_4-type solid acids is that they require active humidification to prevent dehydration and maintain desirable conductivity levels, or stabilize the highly conducting superprotonic phase.[4, 7, 8] Similarly, MOF proton conductors necessitate high RH values or post-synthetic modifications in order to introduce protonic defects and/or vehicular species enabling adequate levels of proton conductivity.[9, 20] In contrast, ZP3 exhibits superprotonic conductivity due to fast transport of native protonic defects under anhydrous conditions. The high anhydrous proton conductivity, and good stability also in alcoholic solutions (Figure S4b), make ZP3 particularly interesting for applications in solid-state electrochemical hydrogen devices operating at low/intermediate temperatures and without the need of humidification.

To investigate the ionic conduction mechanism, the energy landscape for a test H^+ was calculated by the bond-valence sum energy (BVSE) method with the software *soft*BV, [21] using the structural model from Rietveld refinement as input. This method has successfully been employed for the determination of the ionic migration pathways and mechanism in several types of solid ionic conductors. [22] Two lowest energy (0.0 eV absolute BVSE minimum) equilibrium proton positions were identified at Wyckoff position 36*f*, around the non-bridging O2 atoms of the PO_4 tetrahedra (Figure 3a and Figure S6a). H1 is at (~ 0.01, 0.5, ~ 0.99) and H2 at (~ 0.98, ~ 0.79, ~ 0.74). Protons are bistable on two off-centre sites between two O2 atoms which compete as hydrogen bond donor and acceptor due to the short –O2···O2– distance (Figure S6a). [18b, 23, 24] The BVSE analysis shows low energy (< 0.19 eV) connecting isosurfaces across the H1 and H2 positions, indicating 1-dimensional conduction pathways along the hydrogen-bond network (Figure 3a).

Proton migration follows a Grotthuss-like mechanism composed by the rotation (~ 121°) of a proton from the position H1 to H2 (or vice versa) and hopping onto an adjacent O2 atom (Figure 3b). The H1-H2 rotation has the higher activation barrier (*S1*) of 0.182 eV, a value which agrees well with the experimental activation energy. Proton hopping between two adjacent O2 atoms (*S2*) has an almost negligible activation energy (0.007 eV). Proton transfer in ZP3 is fast thanks to the favorable hydrogen-bond network, where the hydrogen atoms are dynamically disordered over two oxygen centres in a symmetric double potential well and can easily interchange their donor and acceptor sites (Figure S6b). [1a, 24] In addition, the particular configuration (six equivalent oxygen sites that are available for five protons) and spatial orientation of the defective 1-dimensional hydrogen bonding arrays create a network of continuous Grotthuss chains running through the entire crystal structure and enabling long-range correlated fast proton motion (Figure 3c). [25] Further neutron

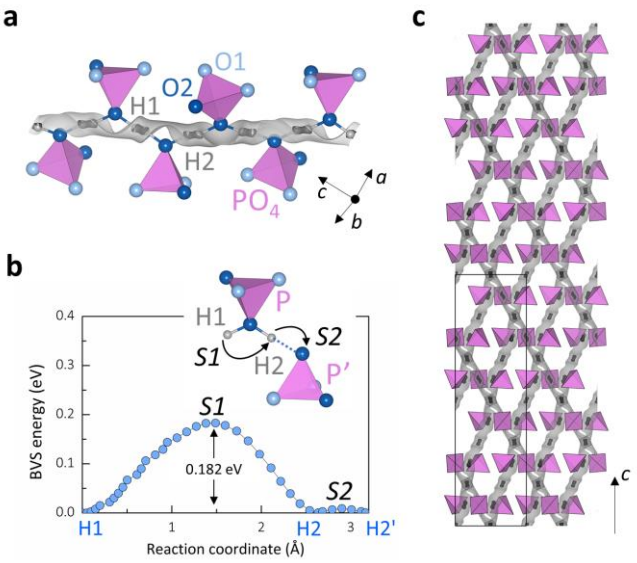

Figure 3. **(a)** BVSE map for a test H^+ (isosurface levels are drawn at < 0.19 eV) showing 1-dimensional connectivity and indicating proton conduction pathways along the terminal O2 oxygen atoms of adjacent phosphate groups. Darker isosurface levels are drawn at 0.0 eV and corresponds to the equilibrium proton positions H1 and H2. **(b)** BVSE barrier and schematic of the proton diffusion mechanism, which is composed by rotation from H1 to H2 (or vice versa) (*S*1) and hopping onto an adjacent terminal O2 atom (*S*2). **(c)** Proton migration network within the ZP3 structure.

scattering experiments will be necessary to confirm the mechanism of fast proton conduction.

In summary, we have synthesized and characterized a new zirconium acid triphosphate, $ZrH_5(PO_4)_3$ (ZP3), exhibiting remarkable superprotonic conductivity under anhydrous conditions. The fast proton transport is due to the particular configuration and spatial orientation of extended hydrogen-bonding chains where protons can readily diffuse. Similar high proton conductivity in anhydrous conditions is observed in the newly synthesized M(IV) related phase $TiH_5(PO_4)_3$ (Figure S7). These results demonstrate that these solid acids constitute a new class of SSPCs with potential applications in low/intermediate temperature hydrogen technologies without the requirement of complex water management systems, as well as for the development of solid-state proton batteries.

ASSOCIATED CONTENT

Supporting Information. The supporting information includes: details of experimental methods; SEM micrographs; results from thermogravimetric analysis; tables of crystallographic data and further structural information; data from solid-state NMR; phase stability results; further conductivity data. This material is available free of charge at http://pubs.acs.org.

AUTHOR INFORMATION

Corresponding Authors

* **Sacha Fop**; orcid.org/0000-0003-4168-6363
Email: sacha.fop1@abdn.ac.uk

* **Anna Donnadio**; orcid.org/0000-0003-2903-4135
Email: anna.donnadio@unipg.it

Authors

Riccardo Vivani; orcid.org/0000-0001-9666-2997

Silvia Masci

Mario Casciola

Notes

The authors declare no competing financial interests.

ACKNOWLEDGMENTS

This paper benefited from the insights of Professor Giulio Alberti who was a pioneer and one of the most authoritative scientists of the chemistry of M(IV) phosphates and phosphonates.

[1] (a) Kreuer, K. Proton Conductivity: Materials and Applications. *Chem. Mater.* **1996***, 8*, 610-641. (b) Norby, T. Solid-State Protonic Conductors: Principles, Properties, Progress and Prospects. *Solid State Ionics* **1999***, 125*, 1-11.

[2] (a) Kreuer, K. Ion Conducting Membranes for Fuel Cells and other Electrochemical Devices. *Chem. Mater.* **2014***, 26*, 361-380. (b) Duan, C.; Tong, J.; Shang, M.; Nikodemski, S.; Sanders, M.; Ricote, S.; Almansoori, A.; O'Hayre, R. Readily Processed Protonic Ceramic Fuel Cells with High Performance at Low Temperatures. *Science* **2015***, 349*, 1321-1326. (c) Duan, C.; Kee, R.; Zhu, H.; Sullivan, N.; Zhu, L.; Bian, L.; Jennings, D.; O'Hayre, R. Highly Efficient Reversible Protonic Ceramic Electrochemical Cells for Power Generation and Fuel Production. *Nature Energy* **2019***, 4*, 230-240. (d) Fop, S. Solid Oxide Proton Conductors Beyond Perovskites. *J. Mater. Chem. A* **2021***, 9*, 18836-18856. (e) Haile, S. M.; Boysen, D. A.; Chisholm, C. R. I.; Merle, R. B. Solid acids as Fuel Cell Electrolytes. *Nature* **2001***, 410*, 910-913. (f) Zhou, Y.; Yang, J.; Su, H.; Zeng, J.; Jiang, S. P.; Goddard, W. A. Insight into Proton Transfer in Phosphotungstic Acid Functionalized Mesoporous Silica-Based Proton Exchange Membrane Fuel Cells. *J. Am. Chem. Soc.* **2014***, 136*, 4954-4964. (g) Li, S.; Xu, Q. Metal–Organic Frameworks as Platforms for Clean Energy. *Energy Environ. Sci.* **2013***, 6*, 1656-1683. (h) Ramaswamy, P.; Wong, N. E.; Shimizu, G. K. H. MOFs as Proton Conductors – Challenges and Opportunities. *Chem. Soc. Rev.* **2014***, 43*, 5913-5932.

[3] (a) Gröger, O.; Gasteiger, H. A.; Suchsland, J. Review—Electromobility: Batteries or Fuel Cells? *J. Electrochem. Soc.* **2015***, 162*, A2605-A2622. (b) Cano, Z. P.; Banham, D.; Ye, S.; Hintennach, A.; Lu, J.; Fowler, M.; Chen, Z. Batteries and Fuel Cells for Emerging Electric Vehicle Markets. *Nature Energy* **2018***, 3*, 279-289. (c) Pollet, B. G.; Kocha, S. S.; Staffell, I. Current Status of Automotive Fuel Cells for Sustainable Transport. *Current Opinion in Electrochemistry* **2019***, 16*, 90-95. (d) Jiao, K.; Xuan, J.; Du, Q.; Bao, Z.; Xie, B.; Wang, B.; Zhao, Y.; Fan, L.; Wang, H.; Hou, Z.; Huo, S.; Brandon, N. P.; Yin, Y.; Guiver, M. D. Designing the Next Generation of Proton-Exchange Membrane Fuel Cells. *Nature* **2021***, 595*, 361-369.

[4] (a) Li, Q.; He, R.; Jensen, J. O.; Bjerrum, N. J. Approaches and Recent Development of Polymer Electrolyte Membranes for Fuel Cells Operating above 100 °C. *Chem. Mater.* **2003***, 15*, 4896-4915. (b) Asensio, J. A.; Sánchez, E. M.; Gómez-Romero, P. Proton-Conducting Membranes Based on Benzimidazole Polymers for High-Temperature PEM Fuel Cells. A Chemical Quest. *Chem. Soc. Rev.* **2010***, 39*, 3210-3239.

[5] Baranov, A. I. Crystals with Disordered Hydrogen-Bond Networks and Superprotonic Conductivity. Review. *Crystallography Reports* **2003***, 48*, 1012-1037.

[6] Haile, S. M.; Chisholm, C. R. I.; Sasaki, K.; Boysen, D. A.; Uda, T. Solid Acid Proton Conductors: from Laboratory Curiosities to Fuel Cell Electrolytes. *Faraday Discuss.* **2007***, 134*, 17-39.

[7] Boysen, D. A.; Uda, T.; Calum, R. I. C.; Haile, S. M. High-Performance Solid Acid Fuel Cells Through Humidity Stabilization. *Science* **2004***, 303*, 68-70.

[8] (a) Wang, L. S.; Patel, S. V.; Sanghvi, S. S.; Hu, Y.; Haile, S. M. Structure and Properties of $Cs_7(H_4PO_4)(H_2PO_4)_8$: A New Superprotonic Solid Acid Featuring the Unusual Polycation $(H_4PO_4)^+$. *J. Am. Chem. Soc.* **2020***, 142*, 19992-20001. (b) Wang, L. S.; Patel, S. V.; Truong, E.; Hu, Y.; Haile, S. M. Phase Behavior and Superprotonic Conductivity in the System $(1–x)CsH_2PO_4 – xH_3PO_4$: Discovery of Off-Stoichiometric α-$[Cs_{1–x}H_x]H_2PO_4$. *Chem. Mater.* **2022***, 34*, 1809-1820.

[9] (a) Hurd, J. A.; Vaidhyanathan, R.; Thangadurai, V.; Ratcliffe, C. I.; Moudrakovski, I. L.; Shimizu, G. K. H. Anhydrous Proton Conduction at 150 °C in a Crystalline Metal–Organic Framework. *Nature Chemistry* **2009***, 1*, 705-710. (b) Ponomareva, V. G.; Kovalenko, K. A.; Chupakhin, A. P.; Dybtsev, D. N.; Shutova, E. S.; Fedin, V. P. Imparting High Proton Conductivity to a Metal–Organic Framework Material by Controlled Acid Impregnation. *J. Am. Chem. Soc.* **2012***, 134*, 15640-15643. (c) Ye, Y.; Zhang, L.; Peng, Q.; Wang, G.; Shen, Y.; Li, Z.; Wang, L.; Ma, X.; Chen, Q.; Zhang, Z.; Xiang, S. High Anhydrous Proton Conductivity of Imidazole-Loaded Mesoporous Polyimides over a Wide Range from Subzero to Moderate Temperature. *J. Am. Chem. Soc.* **2015***, 137*, 913-918. (d) Liu, S.; Yue, Z.; Liu, Y. Incorporation of Imidazole Within the Metal–Organic Framework UiO-67 for Enhanced Anhydrous Proton Conductivity. *Dalton Trans.* **2015***, 44*, 12976-12980. (e) Ye, Y.; Wu, X.; Yao, Z.; Wu, L.; Cai, Z.; Wang, L.; Ma, X.; Chen, Q.; Zhang, Z.; Xiang, S. Metal–Organic Frameworks with a Large Breathing Effect to Host Hydroxyl Compounds for High Anhydrous Proton Conductivity Over a Wide Temperature Range from Subzero to 125 °C. *J. Mater. Chem. A* **2016***, 4*, 4062-4070. (f) Wu, X.; Hong, Y.; Xu, B.; Nishiyama, Y.; Jiang, W.; Zhu, J.; Zhang, G.; Kitagawa, S.; Horike, S. Perfluoroalkyl-Functionalized Covalent Organic Frameworks with Superhydrophobicity for Anhydrous Proton Conduction. *J. Am. Chem. Soc.* **2020***, 142*, 14357-14364.

[10] (a) Lim, D.; Kitagawa, H. Proton Transport in Metal–Organic Frameworks. *Chem. Rev.* **2020***, 120*, 8416-8467. (b) Ye, Y.; Gong, L.; Xiang, S.; Zhang, Z.; Chen, B. Metal–Organic Frameworks as a Versatile Platform for Proton Conductors. *Adv Mater* **2020***, 32*, 1907090. (c) Lim, D.; Kitagawa, H. Rational Strategies for Proton-Conductive Metal–Organic Frameworks. *Chem. Soc. Rev.* **2021***, 50*, 6349-6368.

[11] (a) Capitani, D.; Casciola, M.; Donnadio, A.; Vivani, R. High Yield Precipitation of Crystalline α-Zirconium Phosphate from Oxalic Acid Solutions. *Inorg. Chem.* **2010***, 49*, 9409-9415. (b) Cheng, Y.; Wang, X.; Jaenicke, S.; Chuah, G. Minimalistic Liquid-Assisted Route to Highly Crystalline α-Zirconium Phosphate. *ChemSusChem* **2017***, 10*, 3235-3242. (c) Cheng, Y.; Xiadong Wang, X.; Jaenicke, S.; Chuah, G. Mechanochemistry-Based Synthesis of Highly Crystalline γ-Zirconium Phosphate for Selective Ion Exchange. *Inorg. Chem.* **2018***, 57*, 4370-4378. (d) Kijima, T. Direct Preparation of Theta-Zirconium Phosphate. *Bull. Chem. Soc. Jpn*. **1982**, 55, 3031– 3032. (e) Krogh Andersen, A. M.; Norby, P.; Hanson, J. C.; Vogt, T. Preparation and Characterization of a New 3-Dimensional Zirconium Hydrogen Phosphate, τ-$Zr(HPO_4)_2$. Determination of the Complete Crystal Structure

Combining Synchrotron X-ray Single-Crystal Diffraction and Neutron Powder Diffraction. *Inorg. Chem.* **1998***, 37*, 876-881. (f) Pica, M.; Vivani, R.; Donnadio, A.; Troni, E.; Fop, S.; Casciola, M. Small is Beautiful: The Unusual Transformation of Nanocrystalline Layered α-Zirconium Phosphate into a New 3D Structure. *Inorg. Chem.* **2015***, 54*, 9146-9153.

[12] Favre-Nicolin, V.; Cerný, R. FOX 'Free Objects for Crystallography': A Modular Approach to *Ab Initio* Structure Determination from Powder Diffraction. *Journal of Applied Crystallography* **2002***, 35*, 734-743.

[13] (a) Larson, A. C.; Von Dreele, R. B. General Structural Analysis System (GSAS); Technical Report No. LAUR86-748, Los Alamos National Laboratory **2004**. (b) Toby, B. H. EXPGUI a Graphical User Interface for GSAS. *Journal of Applied Crystallography* **2001***, 34*, 210-213.

[14] Clayden, N. J. Solid-State Nuclear Magnetic Resonance Spectroscopic Study of γ-Zirconium Phosphate. *J. Chem. Soc., Dalton Trans.* **1987**, 1877-1881.

[15] (a) Sadakiyo, M.; Yamada, T.; Honda, K.; Matsui, H.; Kitagawa, H. Control of Crystalline Proton-Conducting Pathways by Water-Induced Transformations of Hydrogen-Bonding Networks in a Metal–Organic Framework. *J. Am. Chem. Soc.* **2014***, 136*, 7701-7707. (b) Sadakiyo, M.; Yamada, T.; Kitagawa, H. Proton Conductivity Control by Ion Substitution in a Highly Proton-Conductive Metal–Organic Framework. *J. Am. Chem. Soc.* **2014***, 136*, 13166-13169. (c) Wei, Y.; Hu, X.; Han, Z.; Dong, X.; Zang, S.; Mak, T. C. W. Unique Proton Dynamics in an Efficient MOF-Based Proton Conductor. *J. Am. Chem. Soc.* **2017***, 139*, 3505-3512.

[16] Haile, S. M.; Liu, H.; Secco, R. A. High-Temperature Behavior of CsH_2PO_4 Under Both Ambient and High Pressure Conditions. *Chem. Mater.* **2003***, 15*, 727-736.

[17] (a) Phang, W. J.; Jo, H.; Lee, W. R.; Song, J. H.; Yoo, K.; Kim, B.; Hong, C. S. Superprotonic Conductivity of a UiO-66 Framework Functionalized with Sulfonic Acid Groups by Facile Postsynthetic Oxidation. *Angew. Chem. Int. Ed.* **2015***, 54*, 5142-5146. (b) Otake, K.; Otsubo, K.; Komatsu, T.; Dekura, S.; Taylor, J. M.; Ikeda, R.; Sugimoto, K.; Fujiwara, A.; Chou, C.; Sakti, A. W.; Nishimura, Y.; Nakai, H.; Kitagawa, H. Confined Water-Mediated High Proton Conduction in Hydrophobic Channel of a Synthetic Nanotube. *Nature Communications* **2020***, 11*, 843.

[18] (a) Gui, D.; Zheng, T.; Xie, J.; Cai, Y.; Wang, Y.; Chen, L.; Diwu, J.; Chai, Z.; Wang, S. Significantly Dense Two-Dimensional Hydrogen-Bond Network in a Layered Zirconium Phosphate Leading to High Proton Conductivities in Both Water-Assisted Low-Temperature and Anhydrous Intermediate-Temperature Regions. *Inorg. Chem.* **2016***, 55*, 12508-12511. (b) Gui, D.; Dai, X.; Tao, Z.; Zheng, T.; Wang, X.; Silver, M. A.; Shu, J.; Chen, L.; Wang, Y.; Zhang, T.; Xie, J.; Zou, L.; Xia, Y.; Zhang, J.; Zhang, J.; Zhao, L.; Diwu, J.; Zhou, R.; Chai, Z.; Wang, S. Unique Proton Transportation Pathway in a Robust Inorganic Coordination Polymer Leading to Intrinsically High and Sustainable Anhydrous Proton Conductivity. *J. Am. Chem. Soc.* **2018***, 140*, 6146-6155. (c) Gui, D.; Zhang, J.; Wang, X.; Wang, C.; Wang, Q.; Zhang, Y.; Li, H.; Wang, S. Ionothermal Synthesis of a Highly Crystalline Zirconium Phosphate Proton Conductor. *Dalton Trans.* **2022***, 51*, 8182-8185.

[19] Casciola, M.; Donnadio, A.; Sassi, P. A Critical Investigation of the Effect of Hygrothermal Cycling on Hydration and In-Plane/Through-Plane Proton Conductivity of Nafion 117 at Medium Temperature (70–130 °C). *J. Power Sources* **2013***, 235*, 129-134.

[20] (a) Taylor, J. M.; Dawson, K. W.; Shimizu, G. K. H. A Water-Stable Metal–Organic Framework with Highly Acidic Pores for Proton-Conducting Applications. *J. Am. Chem. Soc.* **2013***, 135*, 1193-1196. (b) Yang, F.; Xu, G.; Dou, Y.; Wang, B.; Zhang, H.; Wu, H.; Zhou, W.; Li, J.; Chen, B. A Flexible Metal–Organic Framework with a High Density of Sulfonic Acid Sites for Proton Conduction. *Nature Energy* **2017***, 2*, 877-883. (c) Kim, S.; Joarder, B.; Hurd, J. A.; Zhang, J.; Dawson, K. W.; Gelfand, B. S.; Wong, N. E.; Shimizu, G. K. H. Achieving Superprotonic Conduction in Metal–Organic Frameworks through Iterative Design Advances. *J. Am. Chem. Soc.* **2018***, 140*, 1077-1082. (d) Chen, J.; Mei, Q.; Chen, Y.; Marsh, C.; An, B.; Han, X.; Silverwood, I. P.; Li, M.; Cheng, Y.; He, M.; Chen, X.; Li, W.; Kippax-Jones, M.; Crawshaw, D.; Frogley, M. D.; Day, S. J.; García-Sakai, V.; Manuel, P.; Ramirez-Cuesta, A.; Yang, S.; Schröder, M. Highly Efficient Proton Conduction in the Metal–Organic Framework Material $MFM\text{-}300(Cr)\cdot SO_4(H_3O)_2$. *J. Am. Chem. Soc.* **2022***, 144*, 11969-11974.

[21] (a) Chen, H.; Wong, L. L.; Adams, S. SoftBV - a Software Tool for Screening the Materials Genome of Inorganic Fast Ion Conductors. *Acta Crystallographica Section B* **2019***, 75*, 18-33. (b) Wong, L. L.; Phuah, K. C.; Dai, R.; Chen, H.; Chew, W. S.; Adams, S. Bond Valence Pathway Analyzer—An Automatic Rapid Screening Tool for Fast Ion Conductors within softBV. *Chem. Mater.* **2021***, 33*, 625-641.

[22] (a) Zhang, W.; Fujii, K.; Niwa, E; Hagihala, M.; Kamiyama, T.; Yashima, M. Oxide-ion conduction in the Dion–Jacobson phase $CsBi_2Ti_2NbO_{10-\delta}$. *Nat. Commun.* **2020**, *11*, 1224. (b) Murakami, T.; Hester, J. R.; Yashima, M. High Proton Conductivity in $Ba_5Er_2Al_2ZrO_{13}$, a Hexagonal Perovskite-Related Oxide with Intrinsically Oxygen-Deficient Layers. *J. Am. Chem. Soc.* **2020***, 142*, 11653-11657. (c) Wang, K.; Ren, Q.; Gu, Z.; Duan, C.; Wang, J.; Zhu, F.; Fu, Y.; Hao, J.; Zhu, J.; He, L.; Wang, C.; Lu, Y.; Ma, J.; Ma, C. A Cost-Effective and Humidity-Tolerant Chloride Solid Electrolyte for Lithium Batteries. *Nat. Commun.* **2021***, 12*, 4410. (d) Fop, S.; Dawson, J. A.; Fortes, A. D.; Ritter, C.; McLaughlin, A. C. Hydration and Ionic Conduction Mechanisms of Hexagonal Perovskite Derivatives. *Chem. Mater.* **2021***, 33*, 4651-4660. (e) Banik, A.; Zeier, W. G.; Wilkening, H. M. Opening Diffusion Pathways through Site Disorder: The Interplay of Local Structure and Ion Dynamics in the Solid Electrolyte $Li_{6+x}P_{1-x}Ge_xS_5I$ as Probed by Neutron Diffraction and NMR. *J. Am. Chem. Soc.* **2022***, 144*, 1795-1812. (f) Plass, M. A.; Bette, S.; Dinnebier, R. E.; Lotsch, B. V. Enhancement of Superionic Conductivity by Halide Substitution in Strongly Stacking Faulted $Li_3HoBr_{6-x}I_x$ Phases. *Chem. Mater.* **2022***, 34*, 3227-3235.

[23] Kim, G.; Griffin, J. M.; Blanc, F.; Haile, S. M.; Grey, C. P. Characterization of the Dynamics in the Protonic Conductor CsH_2PO_4 by ^{17}O Solid-State NMR Spectroscopy and First-Principles Calculations: Correlating Phosphate and Protonic Motion. *J. Am. Chem. Soc.* **2015***, 137*, 3867-3876.

[24] Katrusiak, A. Geometric Effects of H-atom Disordering in Hydrogen-Bonded Ferroelectrics. *Phys. Rev. B* **1993**, *48*, 2992-3002.

[25] Vilčiauskas, L.; Tuckerman, M. E.; Bester, G.; Paddison, S. J.; Kreuer, K. The Mechanism of Proton Conduction in Phosphoric Acid. *Nature Chemistry* **2012**, *4*, 461-466.

Insert Table of Contents artwork here

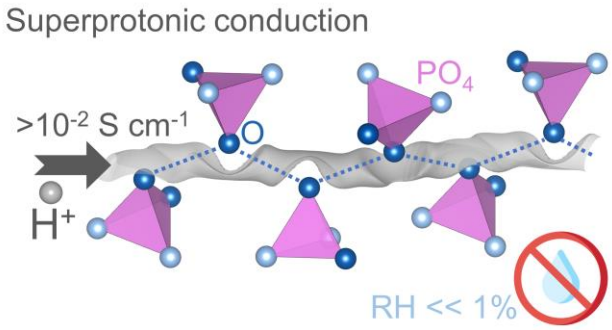

Supplementary Information for

Anhydrous Superprotonic Conductivity in the Zirconium Acid Triphosphate $ZrH_5(PO_4)_3$

Sacha Fop,[1,2,*] Riccardo Vivani,[3,4] Silvia Masci,[5] Mario Casciola,[5] Anna Donnadio,[3,4,*]

[1] The Chemistry Department, University of Aberdeen, Aberdeen AB24 3UE, United Kingdom
[2] ISIS Facility, Rutherford Appleton Laboratory, Harwell OX11 0QX, United Kingdom
[3] Department of Pharmaceutical Sciences, University of Perugia, via del Liceo 1, 06123 Perugia, Italy
[4] CEMIN – Centro di Eccellenza Materiali Innovativi Nanostrutturali per Applicazioni Chimiche, Fisiche e Biomediche, University of Perugia, Via Elce di Sotto 8, 06123, Perugia, Italy
[5] Department of Chemistry, Biology and Biotechnologies, University of Perugia, via Elce di Sotto 8, 06123 Perugia, Italy

* sacha.fop1@abdn.ac.uk

* anna.donnadio@unipg.it

Experimental methods – Further details

Synthesis: Samples of $ZrH_5(PO_4)_3$ (ZP3) were synthesized by precipitation reaction from $ZrOCl_2{\cdot}8H_2O$ (Sigma-Aldrich, 98%) and melted H_3PO_4 (Sigma-Aldrich, crystalline ≥ 99.999% trace metals basis). $ZrOCl_2{\cdot}8H_2O$ was dehydrated at 110°C prior to its use. A stoichiometric quantity of $ZrOCl_2$ was added to melted H_3PO_4 (initial P:Zr molar ratio of 25) under stirring in an open vessel at 85 °C. Full precipitation of a white sample occurred after 1 hour. The mixture was kept under stirring at 85 °C for 48 hours. The resultant solid was isolated by centrifugation, washed with acetone (Sigma-Aldrich, ACS grade ≥ 99.5%) several times (ca. 5 times) in order to remove any excess of phosphoric acid, and finally dried under N_2. After synthesis, the samples were stored under vacuum in the presence of P_2O_5.

Sample analysis: Zirconium and phosphorus contents were obtained by inductively coupled plasma-optical emission spectrophotometry (ICP-OES) using a Varian Liberty Series II instrument working in axial geometry, after the mineralization of the sample with hydrofluoric acid. Thermogravimetric (TGA) measurements were performed on heating the sample using a Netzsch STA490C thermoanalyzer under a 50 mL min^{-1} air flux with a heating rate of 1 °C min^{-1}. Field emission-scanning electron microscopy (FE-SEM) images were collected with a LEO 1525 ZEISS instrument working with an acceleration voltage of 15 kV. Measurements of NH_3 chemisorption were conducted by contacting a weighted amount of ZP3 with a known volume of NH_3 in an evacuated volumetric flask at constant temperature of 25 °C. The system was equilibrated for 24 hours. The final partial pressure of NH_3 in the flask and weight of the ZP3 sample were then used to determine the amount of chemisorbed NH_3 and thus the number of moles of acidic hydrogen atoms. Solid-state ^{31}P MAS-NMR spectra of ZP3 were obtained with a Varian 400 MHz spectrometer at a resonance frequency of 161.97 MHz, employing H_3PO_4 (85% wt.) as external reference

Structure determination and refinement: Powder X-ray diffraction (XRD) patterns for structure determination and Rietveld refinement were collected using a PANalytical X'PERT PRO diffractometer with a Cu Kα tube (operating at 40 kV and 40 mA) and a PW3050 goniometer equipped with an X'Celerator detector. The powder sample was carefully side-loaded onto an aluminum sample holder in order to minimize any preferential orientations of the microcrystals. XRD data were recorded in the range 10° < 2θ < 140°, with a step size of 0.02°.

The crystal structure of ZP3 was solved *ab initio* from powder X-ray diffraction data. Indexing of the XRD pattern was performed using both TREOR90 and the DICVOL06 programs [1, 2]. The indexing procedure gave a trigonal unit cell with lattice parameters a = 8.27325 (3) Å and c = 25.5433 (2) Å. Analysis of the indexed pattern clearly revealed the presence of the following limiting reflection conditions: hkl: $-h + k + l = 3n$; hhl: $l = 3n$; $h\bar{h}l$: $l = 2n$, which suggested $R\bar{3}c$ as the probable space group. The space group was assigned using the CHECKCELL program. The number of formula units contained in the elementary cell (Z) were calculated from the measured sample density (using a solid pycnometer with CCl_4 as reference fluid), according to the relation:

$$\rho = \frac{Z \cdot m}{N_A \cdot V}$$

where ρ is the density, m is molecular mass, N_A is the Avogadro's constant and V is the unit cell volume. This gave Z = 6. An initial structural model was determined using the real space global optimization methods implemented in FOX with the parallel tempering algorithm [3], and subsequently refined with the GSAS/EXPGUI software package [4, 5]. For the Rietveld refinement, the background was fitted with a six-term cosine Fourier series, combined with approximately 50 experimental points, and peak shapes were modelled using a corrected pseudo-Voigt function to take into account the asymmetry at the low angle region. The final refinements were perfomed on all parameters, including fractional atomic coordinates, isotropic displacement parameters, unit cell parameters, zero-shift, background/profile coefficients, and yelded good agreement factors.

Bond-valence site energy analysis: Bond-valence site energy (BVSE) calculations were performed with the *softB*V program [6, 7], using the structural model from Rietveld refinement as input. Bond-valence site energy landscapes for the interaction of test H^+ ion were calculated for a dense grid of points with a resolution of 0.05 Å. Energy minimum equilibrium sites and diffusion pathways were identified with regions of low bond-valence site energy by direct visualization of the isosurfaces and by examination of the calculated energy profiles.

Impedance spectroscopy: The conductivity of ZP3 was measured by AC impedance spectroscopy, with a Solartron 1260 impedance/gain analyzer in the frequency range 10 Hz – 1 MHz with an applied alternating oltage of 0.1 V. Measurements were carried out on a dense pellet (~ 93% of the theoretical density) of approximately ~ 1 mm thickness and ~ 10 mm diameter prepared by pressing ~ 200 mg of sample at 40 kN cm^{-2}. Electrodes were applied by coating both surfaces of the pellet with platinum black (Merck). Measurements were conducted employing an in-house developed stainless steel sealed cell constituted by a sample compartment connected to a water-filled sink, allowing accurate control of the temperature and of the relative humidity (RH) (see ref. 8 for details of the cell). Anhydrous conditions (RH << 1%, $pH_2O << 10^{-2}$ atm) at the sample were obtained by emptying the water sink and filling the compartment with N_2 at 3 °C. Data were taken on heating from 25 to 120 °C in ~ 10 °C steps, with equilibration time of 4 hours at each step. After a first set of measurements, a second set of measurements was taken after cooling and equilibration of the sample at 60 °C for 24 hours.

Determination of H_3PO_4: In order to check any possible contribution of H_3PO_4 (which could have been formed at the grain boundary during the preparation of the pellet sample) to the proton conductivity, a ZP3 pellet was ground and the obtained powder was thoroughly washed with anhydrous acetone. The amount of phosphoric acid released (determined by ICP-OES) was 3.4 mg per g of ZP3, corresponding to 4.5 x 10^{-3} mL of phosphoric acid ($\rho_{25\,°C}$ = 1.88 g cm^{-3}) per 1 mL of ZP3. Therefore, considering that the pellet relative density is lower than 1, the H_3PO_4 volume fraction in the ZP3 pellet ($x_{H_3PO_4}$) is at most 4.5 x 10^{-3}. The maximum contribution of phosphoric acid to the pellet conductivity ($\sigma_{H_3PO_4\ MAX}$) is given by the product: $x_{H_3PO_4} \cdot \sigma_{H_3PO_4}$. If it is assumed that the conductivity of free H_3PO_4 in the pellet is the same as that in liquid H_3PO_4, then $\sigma_{H_3PO_4}$ = 0.127 S cm^{-1} at 60°C [9], therefore $\sigma_{H_3PO_4\ MAX}$ = 6 x 10^{-4} S cm^{-1}. This value corresponds to ~ 5% of the pellet conductivity at 60°C and constitutes the upper limit of any

possible contribution of H_3PO_4 to the proton conductivity of ZP3. This value also suggests that if the conductivity of ZP3 was purely due to the presence of H_3PO_4, then it should be inferred that the conductivity of H_3PO_4 adsorbed at the grain boundaries of the ZP3 crystals is higher than the conductivity of liquid H_3PO_4 by a factor of 20. This is clearly unrealistic and indicates that the high ionic conductivity of ZP3 is due to fast proton transport within the bulk material.

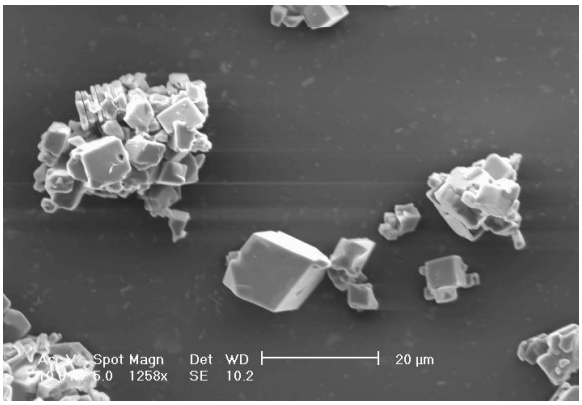

Figure S1. SEM micrograph of as-prepared ZP3 crystals. ZP3 presents crystals with cubic-like morphology and dimensions of about 5 – 10 µm.

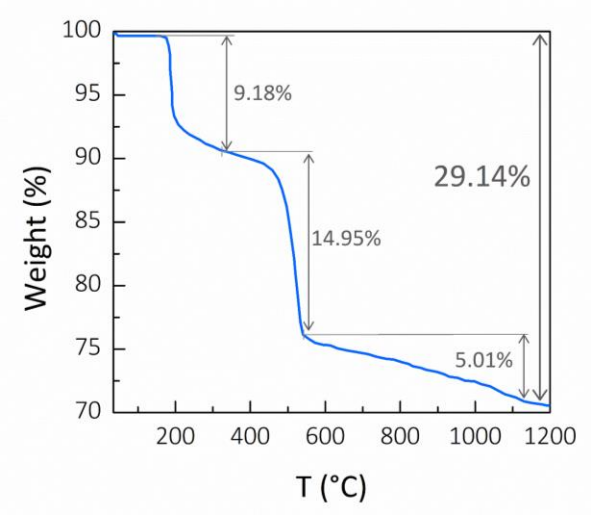

Figure S2. Results from thermogravimetric analysis (TGA) on ZP3.

Heating ZP3 up to 1200°C leads to the formation of cubic ZrP_2O_7, which also implies the formation of water and P_2O_5 according to the reaction:

$$ZrH_5(PO_4)_3 \rightarrow ZrP_2O_7 + 0.5\ P_2O_5 + 2.5\ H_2O$$

The weight loss predicted on the basis of the loss of water and the sublimation of P_2O_5 (30.44%) fairly agrees with the observed weight loss (29.14%). In particular, the sample undergoes a first weight loss between 180 and 300°C, which can be ascribed to the condensation of the P–OH groups and the concomitant loss of 1.9 moles of H_2O, leading to the formation of ZrP_2O_7 and P_2O_5. This is followed by a second loss in the range 300 – 550 °C and by a slow downward drift up to 1200 °C due to the loss of the residual water (0.6 moles) and the slow sublimation of P_2O_5.

Table S1. Crystal data and refined atomic parameters from Rietveld fit of the high-resolution X-ray diffraction data of ZP3 collected at room temperature (25 °C). All atoms were refined with isotropic displacement parameters, U_{iso} (Å^2).

Formula		$ZrH_5(PO_4)_3$	
Crystal system		Trigonal	
Space group		$R\bar{3}c$ (No. 167)	
Z		6	
ρ		2.51 g cm^{-3}	
Unit cell parameters			
	***a* (Å)**	8.27299(4)	
	***c* (Å)**	25.5426(2)	
	***V* (Å^3)**	1513.98(1)	
Atomic parameters			
Zr1	**6*b* (0,0,0)**	U_{iso}	0.0139(2)
P1	**18*e* (*x*,0, ¼)**	***x***	0.6687(3)
		U_{iso}	0.0355(5)
O1	**36*f* (*x*,*y*,*z*)**	***x***	0.5108(4)
		y	0.8902(4)
		z	0.2130(1)
		U_{iso}	0.026(1)
O2	**36*f* (*x*,*y*,*z*)**	***x***	0.7193(6)
		y	0.8754(5)
		z	0.2815(1)
		U_{iso}	0.072(2)
Statistics			
	χ^2		2.6
	R_p		0.084
	R_{wp}		0.110
	R_F2		0.103

Table S2. Selected bond lengths and angles for ZP3.

Bond (Å)	
Zr1–O1	2.059(3)
P1–O1	1.496(3)
P1–O2	1.525(4)
O2···O2	2.756(2)
	2.762(2)
O2–H1[a]	1.100(1)
O2–H2[a]	1.050(1)
Angle (°)	
O1–Zr1–O1	91.1(1)
	180
	88.9(1)
O1–P1–O1	112.5(3)
O1–P1–O2	112.3(2)
	107.7(2)
O2–P1–O2	104.2(3)

[a] Obtained from the BVSE calculations.

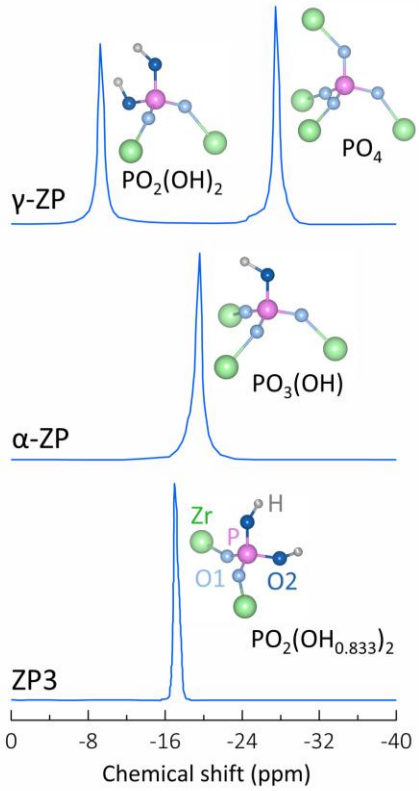

Figure S3. Solid-state ^{31}P MAS NMR spectrum of ZP3 with an illustration showing the local coordination of the phosphate group. The semi filled grey spheres represent partially occupied hydrogen sites. The ^{31}P MAS NMR spectra of α-$Zr(HPO_4)_2{\cdot}H_2O$ (α-ZP) and γ-$Zr(PO_4)(H_2PO_4){\cdot}2H_2O$ (γ-ZP), with the relative local phosphate coordinations, are also shown for comparison (data taken from ref. 10).

The spectrum of ZP3 shows a single sharp resonance, demonstrating the presence of a single type of phosphate group [10, 11]. This is analogous to the case of α-ZP, which presents a single $PO_3(OH)$ group, and in contrast with γ-ZP, which shows two resonances for the two chemically distinct $PO_2(OH)_2$ and PO_4 groups. In solid acid zirconium phosphates, substitution of Zr by H in the local coordination of the phosphate groups causes a downfield shift of about 10 ppm in the ^{31}P chemical shift due to a decrease in the P–O bond strength [10]. Therefore, in α-ZP the $PO_3(OH)$ signal is at ca. -19 ppm, while in γ-ZP the $PO_2(OH)_2$ signal is at ca. -9 ppm and the PO_4 signal at ca. -29 ppm. The sharp resonance in the spectrum of ZP3 is at ca. -17 ppm, somehow in between what expected for the presence of $PO_3(OH)$ or $PO_2(OH)_2$ groups. Combined with the existence of a single type of phosphate group, this evidences that in ZP3 the five protons per formula unit are delocalized on six equivalent non-coordinated oxygen atoms (two per phosphate group), resulting in a defective phosphate group $PO_2(OH_{0.83})_2$.

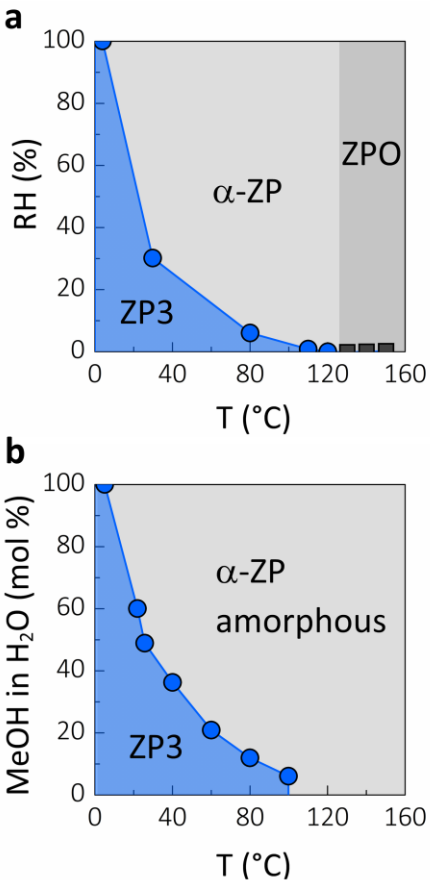

Figure S4. (a) Phase diagram for ZP3. The phase stability was identified by maintaining the sample at controlled temperatures and RH values in sealed containers for 144 hours (6 days). ZP3 converts into crystalline α-$Zr(HPO_4)_2 \cdot H_2O$ (α-ZP) when exposed to humid environments at high temperatures, while it transforms into pyrophosphate ZrP_2O_7 (ZPO) in dry conditions above 130 °C. **(b)** Phase stability diagram of ZPR in solutions of MeOH in H_2O. ZP3 is stable in anhydrous alcoholic solutions below 100 °C. ZP3 converts into amorphous α-ZP at higher temperatures and concentrations of water.

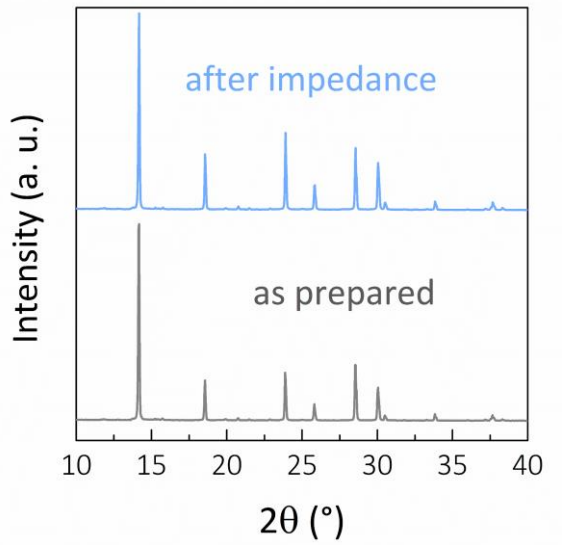

Figure S5. X-ray diffraction patterns of as prepared ZP3 and after the impedance spectroscopy measurements. No changes or parasitic phases are detectable from the diffraction pattern collected post-conductivity measurements, thus confirming the good stability of ZP3.

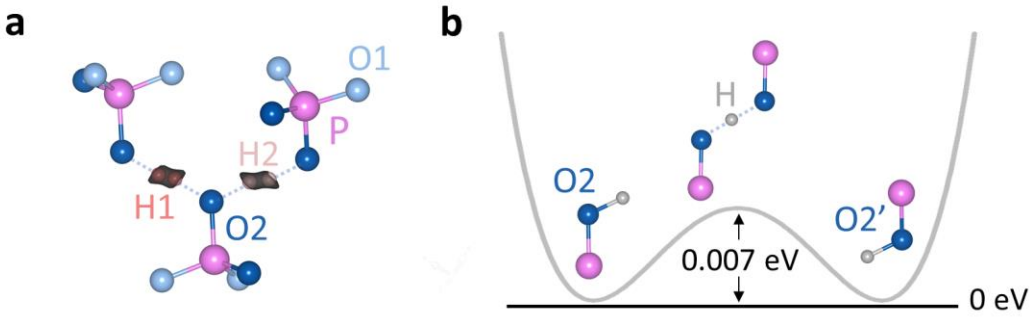

Figure S6. (a) Bond-valence site energy isosurfaces showing the lowest energy equilibrium proton positions H1 and H2 (isosurface levels are drawn at 0.0 eV). Protons are bistable on two off-centre sites between two O2 atoms which compete as hydrogen bond donor and acceptor. Crystallographycally, the individual H1 and H2 sites must be partially occupied with *g*(H1, H2) = 0.41667. **(b)** Representation of the symmetric double potential well resulting from the disordered proton configuration over two oxygen O2 centers. Protons transfer between two adjacent O2 atoms is favored due to the low activation energy (0.007 eV) for donor/acceptor interchange in the hydrogen bond [12, 13].

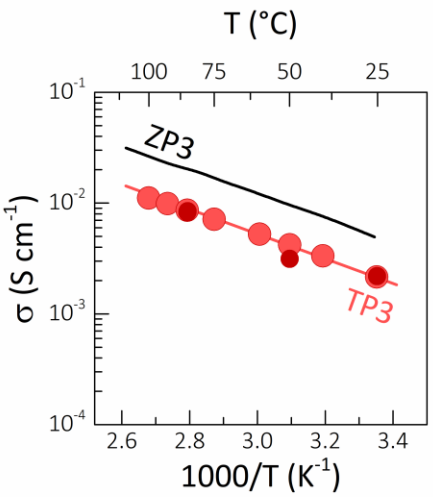

Figure S7. Arrhenius plot of the conductivity of $TiH_5(PO_4)_3$ (TP3) compared with the conductivity of ZP3. Darker filled symbols are the data taken after a second cooling and heating cycle.

References

[1] Werner, P. -.; Eriksson, L.; Westdahl, M. TREOR a Semi-Exhaustive Trial-And-Error Powder Indexing Program for All Symmetries. *Journal of Applied Crystallography* **1985***, 18*, 367-370.

[2] Boultif, A.; Louër, D. Powder Pattern Indexing with the Dichotomy Method. *Journal of Applied Crystallography* **2004***, 37*, 724-731.

[3] Favre-Nicolin, V.; Cerný, R. FOX 'Free Objects for Crystallography': A Modular Approach to *Ab Initio* Structure Determination from Powder Diffraction. *Journal of Applied Crystallography* **2002***, 35*, 734-743.

[4] Toby, B. H. EXPGUI a Graphical User Interface for GSAS. *Journal of Applied Crystallography* **2001***, 34*, 210-213.

[5] Larson, A. C.; Von Dreele, R. B. General Structural Analysis System (GSAS); Technical Report No. LAUR86-748, Los Alamos National Laboratory **2004**.

[6] Chen, H.; Wong, L. L.; Adams, S. SoftBV - a Software Tool for Screening the Materials Genome of Inorganic Fast Ion Conductors. *Acta Crystallographica Section B* **2019***, 75*, 18-33.

[7] Wong, L. L.; Phuah, K. C.; Dai, R.; Chen, H.; Chew, W. S.; Adams, S. Bond Valence Pathway Analyzer—An Automatic Rapid Screening Tool for Fast Ion Conductors within softBV. *Chem. Mater.* **2021***, 33*, 625-641.

[8] Alberti, G.; Casciola, M.; Massinelli, L.; Bauer, B. Polymeric Proton Conducting Membranes for Medium Temperature Fuel Cells (110–160°C). *J. Membr. Sci.* **2001***, 185*, 73-81.

[9] Greenwood, N. N.; Thompson, A. 701. The Mechanism of Electrical Conduction in Fused Phosphoric and Trideuterophosphoric Acids. *J. Chem. Soc.* **1959**, 3485-3492.

[10] Clayden, N. J. Solid-State Nuclear Magnetic Resonance Spectroscopic Study of γ-Zirconium Phosphate. *J. Chem. Soc., Dalton Trans.* **1987**, 1877-1881.

[11] Jakeman, R. J. B.; Cheetham, A. K.; Clayden, N. J.; Dobson, C. M. Phosphorus-31 Magic Angle Spinning NMR Study of the Cation Distribution in $Zn_{3-x}Mg_x(PO_4)_2$. *J. Am. Chem. Soc.* **1985***, 107*, 6249-6252.

[12] Kreuer, K. Proton Conductivity: Materials and Applications. *Chem. Mater.* **1996***, 8*, 610-641.

[13] Katrusiak, A. Geometric Effects of H-atom Disordering in Hydrogen-Bonded Ferroelectrics. *Phys. Rev. B* **1993***, 48*, 2992-3002.